Coherence-Induced Bias Reduction in Synthetic Aperture Sonar Along-Track Micronavigation

Benjamin Thomas and Alan Hunter, *Senior Member, IEEE*

Abstract

Sub-wavelength motion estimation is vital for the production of focused synthetic aperture sonar (SAS) imagery. The required precision is obtainable from the sonar data itself through a process termed micronavigation. Along-track micronavigation is achieved by a similar technique to that used in correlation velocity logs (CVLs), where sparse estimates of the spatial coherence function are interpolated to estimate the location of the peak coherence and hence estimate the inter-ping vehicle motion. However, along-track micronavigation estimates made using this technique are biased, which limits the utility of these measurements for long-term navigation of autonomous underwater vehicles (AUVs).

Three sources of along-track motion estimation bias are considered in this paper. Firstly, imperfect temporal registration between the signals results in coherence estimates that are negatively biased as a function of the temporal offset. Secondly, the sparse estimates of the spatial coherence function are obtained by cross-correlation of complex baseband signals, a process which is known to result in positively biased coherence estimates, especially when the true coherence is low. Finally, mismatches between the underlying spatial coherence function and the interpolation kernel used to estimate the peak coherence location also result in along-track micronavigation bias.

In this paper we describe and evaluate three methods for reducing along-track micronavigation bias. We introduce a temporal registration of the signals prior to coherence estimation, which reduces the impact of negative coherence bias due to temporal offsets. The remaining coherence estimation bias is reduced by combining multiple coherence estimates in a Bayesian coherence estimator. Additionally, an improved interpolation kernel is derived with a significantly improved fit compared to the current gold standard Gaussian interpolation kernel.

The improvements in along-track micronavigation accuracy are demonstrated using two simulated datasets, which both allow comparison with ground truth. The first involves direct simulation of the spatial coherence from a given inter-ping geometry using the pulse-echo formulation of the van Cittert-Zernike theorem, while the second involves simulation of raw sonar echo data using a point scatterer model. Using these simulations, a reduction in along-track micronavigation bias of 48.5 - 99.5% is demonstrated, with reductions in along-track micronavigation error standard deviation of up to 34%. This improvement expands the potential for SAS-equipped AUVs to reduce their long-term navigation drift, facilitating longer underwater transits, improved target localisation and reduced track misalignment in repeat-pass operations.

Benjamin Thomas and Alan Hunter are with the University of Bath, UK

Manuscript received Month Day, Year; revised Month Day, Year.

Coherence-Induced Bias Reduction in Synthetic Aperture Sonar Along-Track Micronavigation

I. Introduction

Localisation of autonomous underwater vehicles (AUVs) is typically achieved by optimal fusion and integration of measurements made by high precision inertial navigation systems (INSs) consisting of accelerometers, gyroscopes and magnetometers, and an aiding sensor such as a doppler velocity log (DVL). One such state-of-the-art system, the iXblue Phins Subsea, is quoted to achieve DVL-aided positioning accuracy of 0.05% of distance travelled in a straight line [1]. However, the short-term precision is typically insufficient for AUVs equipped with synthetic aperture sonar (SAS) systems to form adequately focused images. This has led to the use of through-the-sensor navigation estimation algorithms, commonly referred to as 'micronavigation,' that exploit redundant data collected between adjacent pings to achieve the sub-wavelength precision required for synthetic aperture image formation.

Along-track motion estimates in redundant phase centre (RPC) micronavigation are obtained by estimating the degree of coherence between signals received by the subset of phase centre pairs around an a-priori inter-ping motion estimate. The location of the phase centre pair with highest coherence gives a coarse estimate of sensor advance. Interpolating this sparsely sampled set of coherence estimates in the along-track direction allows the location of the peak coherence to be found as a fraction of a phase centre spacing, which refines the coarse along-track motion estimate. This method was first described by Dickey for velocity estimation of aircraft using radar [2], [3] and later for ships using sonar [4], [5].

The high precision achieved by through-the-sensor navigation estimation algorithms suggests there is potential for SAS micronavigation estimates to be used to improve the long-term navigation accuracy and precision of AUVs [6]. This would allow AUVs to perform longer underwater transits, improve geo-location accuracy of SAS images, and enable repeated passes to be made with improved accuracy. This enticing potential was noted in 2003 by Gough and Miller [7], who suggested that *"it could be possible that sometime in the future, all AUVs will be deployed with an array SAS on board not for imaging, but for navigation"*.

Limited attempts have been made to realise this potential to date. In an experimental trial [8], a disparity was identified between micronavigation estimates and INS estimates in both the along-track and across-track directions. While it is suggested that the across-track disparity can be explained by a misalignment between the SAS and the INS, no explanation is given for the along-track disparity. We suggest that this disparity was likely caused by a combination of 1) the fact that coherence estimates between complex baseband signals are known to be biased [9]–[13], 2) the use of an interpolation kernel with poor correspondence to the spatial coherence function [14], and 3) the along-track motion estimation bias caused by relative inclination of the SAS with respect to the seafloor [6]. In this paper, we investigate the along-track micronavigation bias caused by coherence biases and mismatches between the interpolation kernel and the spatial coherence function. Investigation of the effect of relative inclination

of the SAS and seafloor is reserved for future work. In Section II we provide a review of the conventional approach to along-track motion estimation using redundant signals, and in Section II-A we identify the sources of bias that are inherent to this method: coherence biases and interpolation kernel bias. Section III reviews the definition and statistics of the coherence magnitude between complex baseband signals, and Sections III-A and III-B provide two methods which combine to reduce the coherence bias; a temporal registration and a Bayesian approach to residual bias reduction. In Section IV we review the van Cittert-Zernike theorem for pulse-echo signals derived by Brown [12] and derive an improved interpolation kernel function. The various bias sources and compensation methods are summarised in Table I. In Section V we quantify the resulting reduction in along-track micronavigation bias using two simulated datasets. The first is based on direct simulation of coherence samples using the van Cittert-Zernike theorem, from which along-track micronavigation estimates are made and compared with ground truth. The second method implements a full along-track micronavigation processing chain using simulated raw echo data from a point scatterer model. Simulated data such as these are preferred over experimental data from fielded SAS systems for this work for multiple reasons, not least because it enables direct comparison of individual inter-ping micronavigation estimates with ground truth. Importantly, it also allows the multiple sources of micronavigation biases to be decoupled under ideal conditions; in this case the effect of relative inclination between the SAS array and the ensonified seafloor [6] has been neglected by simulating a horizontal seafloor and a perfectly linear collection geometry.

Bias source	Gold standard correction method	Proposed correction method	Impact
Temporal misregistration	Non-zero lag cross-correlation to approximate sample coherence	**Delay and yaw compensation** (Section III-A)	Accurate sample coherence estimation by zero-lag cross-correlation Reduced along-track micronavigation bias
Zero-lag coherence bias	Use of large estimation windows	**Bayes coherence estimation** (Section III-B)	Reduced coherence bias with shorter estimation windows for improved inter-ping sway and heave tolerance
Interpolation kernel mismatch	Gaussian interpolation kernel [14]	**Cubic interpolation kernel** (Section IV)	Reduced along-track micronavigation bias

TABLE I: A summary of the proposed methods for along-track micronavigation bias reduction and their impacts.

II. Along-track Micronavigation

Estimation of the along-track displacement of a SAS between successive pings is analogous to the operation of a uni-directional correlation velocity log (CVL), as has been described previously in [14]–[17]. We review the method here for systems with uniformly spaced receiver array elements to clarify our implementation of the procedure and to identify the steps at which various biases are introduced.

Consider a pair of successive pings $\{p \in [p_1, p_2]\}$, between which the foremost phase centres[1] from ping p_1

[1]The array of phase centres has elements located at the midpoint of the transmitter and each receive element. Phase centres are frequently used to approximate a bistatic sensor array as an array of monostatic transducers.

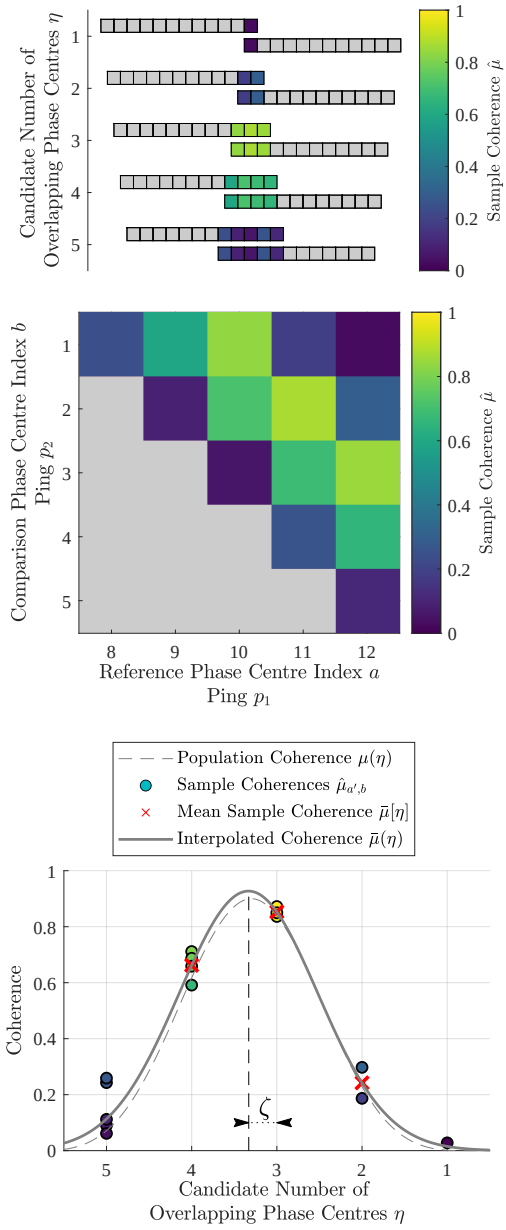

Fig. 1: Along-track SAS micronavigation. (a) Coherence is estimated between signals received by phase centre pairs for a range of potential phase centre overlaps. (b) In regions of favourable coherence, the matrix of coherence estimates has high values along a diagonal. (c) The mean coherence is taken over the diagonals of (b) and the maximum coherence location is estimated by fitting an interpolation kernel to the peak and its adjacent samples.

overlap with the aftmost phase centres from ping p_2. The signals received by the phase centres are denoted $s_{a,p}[t]$ where a denotes the phase centre index and $t = \{n\Delta t \mid n \in [0, ..., N_s - 1]\}$ where $\Delta t = 1/f_s$ is the sample period at sampling frequency f_s, N_s is the number of samples and t is time. These signals are windowed in time such that each window corresponds to a subset of the swath in range by

$$s_{a,p,q}[t] = s_{a,p}[t] \operatorname{rect}\left(\frac{t - t_q}{\tau}\right) \tag{1}$$

where $\tau = N_w/B$ is the temporal window length corresponding to the number of samples in the temporal window N_w for frequency bandwidth B. The centre of the temporal window is given by $t_q = 2R_q/c$ at range R_q for sound speed c. The rectangular windowing function is defined by

$$\operatorname{rect}(x) = \begin{cases} 0, \text{ if } |x| > \frac{1}{2} \\ \frac{1}{2}, \text{ if } |x| = \frac{1}{2} \\ 1, \text{ if } |x| < \frac{1}{2} \end{cases} . \tag{2}$$

The inter-ping sample coherence between the range windowed signals is estimated between candidate phase centre pairs, as demonstrated in Figure 1a. These sample coherences are populated into the matrix

$$\hat{\boldsymbol{\mu}}_q = \begin{bmatrix} \hat{\mu}_{1,1} & \dots & \hat{\mu}_{1,A} \\ \vdots & \hat{\mu}_{a,b} & \vdots \\ \hat{\mu}_{A,1} & \dots & \hat{\mu}_{A,A} \end{bmatrix}, \tag{3}$$

shown in Figure 1b, where A is the number of receivers in the array, $\hat{(\cdot)}$ denotes an estimate and where sample coherence is defined as the zero-lag cross-correlation coefficient given by

$$\hat{\mu}_{a,b} = \left| \frac{\sum_t s_{a,p_1,q}[t] s^*_{b,p_2,q}[t]}{\sqrt{\sum_t |s_{a,p_1,q}[t]| \sum_t |s_{b,p_2,q}[t]|}} \right|. \tag{4}$$

Typically, only a subset of the matrix of sample coherences $\hat{\boldsymbol{\mu}}_q$ must be populated, since approximate a-priori knowledge of the platform velocity is often available from the vehicle navigation system.

This definition of the degree of coherence is only a valid measure of spatial coherence for time-aligned signals, which is rarely the case in practice due to inter-ping sway, inter-ping yaw and crabbing motions. The typical workaround involves computing the normalised cross-correlation [17] given by

$$\hat{\rho}_{a,b}[\tau] = \frac{s_{a,p_1,q}[t] \star s_{b,p_2,q}[t]}{\sqrt{\sum_t |s_{a,p_1,q}[t]| \sum_t |s_{b,p_2,q}[t]|}} \tag{5}$$

where

$$(x_1 \star x_2)[\tau] \equiv \sum_{\tau=-\infty}^{\infty} x_1^*[t] x_2[t + \tau] \tag{6}$$

defines cross-correlation and $(\cdot)^*$ denotes conjugation. This normalised cross-correlation is conveniently computed in the Fourier domain as

$$(x_1 \star x_2)[\tau] \equiv \mathcal{F}^{-1}\left\{X_1^*[f] X_2[f]\right\} \tag{7}$$

where $X_i[f] = \mathcal{F}\left\{x_i[t]\right\}$, with $\mathcal{F}\left\{\cdot\right\}$ denoting the Fourier transform operator. However, it should be noted that the definition in (7) performs a circular cross-correlation, while (5) does not.

We now replace the matrix of sample coherences $\hat{\boldsymbol{\mu}}_q$ with the matrix

$$\hat{\boldsymbol{\rho}}_q = \begin{bmatrix} \hat{\rho}_{1,1} & \cdots & \hat{\rho}_{1,A} \\ \vdots & \hat{\rho}_{a,b} & \vdots \\ \hat{\rho}_{A,1} & \cdots & \hat{\rho}_{A,A} \end{bmatrix}, \tag{8}$$

whose elements are the maximum of the normalised cross-correlation in (5) over a subset of temporal lags for each phase centre pair,

$$\hat{\rho}_{a,b} = \max_{\tau'} \left\{ \left| \hat{\rho}_{a,b}\left[\tau\right] \right| \right\}, \tag{9}$$

where $\tau' = \{n\Delta t \mid n \in [-n_{\max}, ..., n_{\max}]\}$ is the subset of temporal lags where $n_{\max}$ is the maximum absolute sample lag.

Having populated the relevant subset of $\hat{\boldsymbol{\rho}}_q$, the mean across the diagonal elements is taken by

$$\bar{\rho}[\eta] = \sum_{b=1}^{\eta} \frac{\hat{\rho}_{a',b}}{\eta} \tag{10}$$

where $a' = A - (\eta - b)$ and $\{\eta \in [1, ..., A]\}$ is the vector of candidate phase centre overlaps and the range window index q has been dropped for clarity in the following. The location of the maximum along this vector,

$$\hat{\eta} = \arg\max_{\eta} \left\{ \bar{\rho}[\eta] \right\} \tag{11}$$

gives an estimate of the closest integer number of overlapping phase centres.

This estimate is then refined by means of interpolation, using the three samples that represent the peak of $\bar{\rho}[\eta]$, namely $\bar{\rho}[\hat{\eta}-1]$, $\bar{\rho}[\hat{\eta}]$ and $\bar{\rho}[\hat{\eta}+1]$, with shorthand ρ_{-1}, ρ_0 and ρ_1 respectively in (13-15). The sub-sample estimate for the location of the peak coherence is given by finding the parameters of an interpolation kernel that passes through these points. Interpolation kernels in the literature include a quadratic [16], [18], a triangular function [19] and a Gaussian [19], [20]. Currently, the *gold standard* is the Gaussian interpolation kernel, which has been shown to improve SAS image quality both qualitatively and quantitatively when compared to the quadratic kernel [14] and to reduce along-track motion estimation bias when compared to both the triangular interpolation kernel [19] and the quadratic interpolation kernel [14]. The Gaussian interpolation kernel takes the form [14]

$$\mu(x) = \mu_0 \exp\left\{ -\frac{1}{2} \frac{(x-\zeta)^2}{\sigma^2} \right\} \tag{12}$$

where μ_0 is the peak coherence, σ defines the kernel width, ζ is the peak offset and x, ζ and σ are in the non-dimensional units of phase centre spacings. The peak offset estimate is given by the three-point interpolation formula [14]

$$\hat{\zeta} = \frac{1}{2} \frac{\ln(\rho_{-1}) - \ln(\rho_1)}{\ln(\rho_{-1}) - 2\ln(\rho_0) + \ln(\rho_1)}, \tag{13}$$

the peak coherence estimate is given by

$$\hat{\mu}_0 = \exp\left\{ \frac{\ln(\rho_{-1})^2 + 16\ln(\rho_0)^2 + \ln(\rho_1)^2 - 8\ln(\rho_{-1})\ln(\rho_0) - 2\ln(\rho_{-1})\ln(\rho_1) - 8\ln(\rho_0)\ln(\rho_1)}{-8\left(\ln(\rho_{-1}) - 2\ln(\rho_0) + \ln(\rho_1)\right)} \right\} \tag{14}$$

and the kernel width estimate is given by

$$\hat{\sigma} = \frac{1}{\sqrt{\ln(\rho_{-1}) - 2\ln(\rho_0) + \ln(\rho_1)}}, \tag{15}$$

which can be interpreted as a non-dimensional measure of spatial coherence length. The sub-sample estimate for the number of overlapping phase centres at each temporal window is then given by

$$\hat{\psi} = \hat{\eta} + \hat{\zeta} \tag{16}$$

and finally, the along-track motion estimate $\hat{\xi}$ is given for each temporal window by

$$\hat{\xi} = \left(A - \hat{\psi}\right) \frac{\Delta}{2} \tag{17}$$

where Δ is the distance between elements in the receiver array.

A. Sources of Motion Estimation Bias

Populating $\hat{\boldsymbol{\mu}}_q$ with the maximum of the normalised cross-correlation over multiple lags in place of the zero-lag normalised cross-correlation does improve robustness to temporal offsets between the signals. However, there are problems with this approach, not limited to the extra computational expense involved noted by Cook [17]. Firstly, the true peak of the cross-correlation function is only sampled if the time delay between signals is equal to an integer multiple of the sampling period. Moreover, the maximum of the normalised cross-correlation over multiple lags is a biased estimator of coherence. Nevertheless, even when the coherence is correctly computed as the zero-lag correlation coefficient as in (4), the coherence estimates are still biased towards larger values, particularly at low coherence. In the following, we refer to these biases as the 'non-zero lag coherence bias' and the 'zero-lag coherence bias'.

These biases are demonstrated in Figure 2, which shows the result of computing the maximum of the normalised cross-correlation function over a range of maximum absolute temporal lags and population coherence values. The coherence estimate bias shown is the median error between the population coherence and the coherence estimate over a Carlo simulation of Gaussian-distributed circular complex signals with length $n = 120$ samples. The estimation bias is most pronounced for low values of population coherence and when the maximum absolute temporal lag is non-zero. However, even the zero-lag normalised cross-correlation exhibits a bias, particularly at low values of population coherence. In Section III-A we present a method to eliminate the non-zero lag coherence bias by temporal registration prior to computing the zero-lag coherence using (4). In Section III-B we present a method to mitigate the zero lag coherence bias, which involves Bayesian estimation of population coherence over multiple sample coherence estimates.

While a Gaussian interpolation kernel is a considerably better fit to the along-track spatial coherence function than a quadratic [14], errors remain between the Gaussian function and the true along-track spatial coherence function. We observe that this mismatch results in biased along-track motion estimates. In Section IV, we derive an improved interpolation kernel and demonstrate the improved fit it offers.

III. Minimising Coherence Bias

The degree of coherence between two signals $x_1(t)$ and $x_2(t)$ is defined as [21]

$$\mu \equiv \frac{\mathbb{E}\{x_1(t)x_2(t)^*\}}{\sqrt{\mathbb{E}\left\{|x_1(t)|^2\right\}\mathbb{E}\{|x_2(t)|^2\}}}, \tag{18}$$

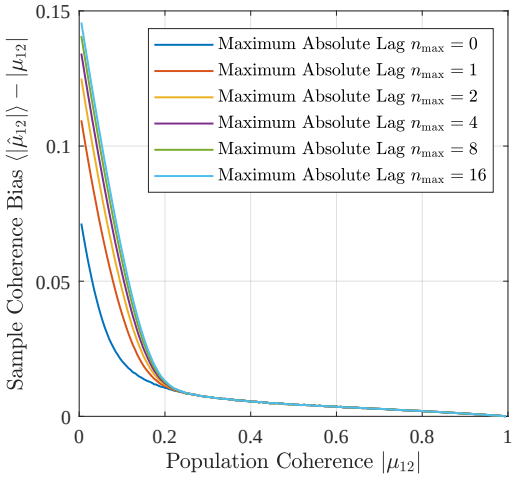

Fig. 2: The coherence estimate bias when the maximum of the normalised cross-correlation function over a subset of temporal lags used as a coherence estimate between Gaussian distributed signals of length $n = 120$. Significant bias is seen at low values of population coherence and high maximum absolute temporal lag.

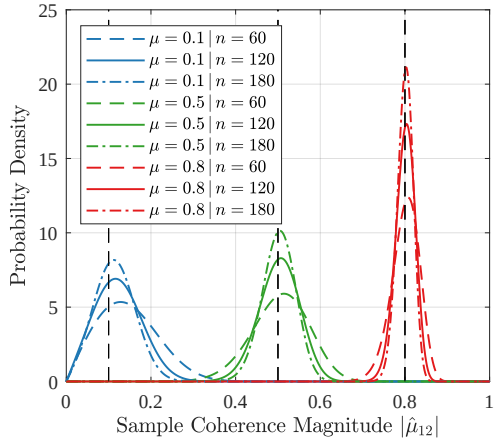

Fig. 3: Example sample coherence probability density functions given population coherence $\{\mu_{12} \in [0.1, 0.5, 0.8]\}$ and number of independent samples $\{n \in [60, 120, 180]\}$.

where $\mathbb{E}\{\cdot\}$ represents the expectation operator. For discrete signals, the maximum likelihood estimate of the coherence magnitude is given by

$$\hat{\mu} = \left| \frac{\sum_t x_1[t] x_2[t]^*}{\sqrt{\sum_t |x_1[t]| \sum_t |x_2[t]|}} \right|, \tag{19}$$

which is the magnitude of the sample coherence over these finite-length signals.

For a pair of jointly complex circular Gaussian processes, the probability density function of the sample coherence magnitude $\hat{\mu}$ given the population coherence μ and the number of independent samples n has been derived by Carter and Nuttall [22] and Touzi and Lopez [10] as

$$\mathrm{P}(\hat{\mu};\mu,n) = 2(n-1)(1-\mu^2)^n\hat{\mu}(1-\hat{\mu}^2)^{n-2}{}_2F_1(n,n;1,\mu^2\hat{\mu}^2), \tag{20}$$

where ${}_2F_1$ denotes the Gauss hypergeometric function[2] [23]. Examples of this probability density function (PDF) are shown in Figure 3 for a variety of values of μ and n. The moments $\{m_k \mid k \in \mathbb{Z}^+\}$ of this PDF are given by [11]

$$m_k = \frac{\Gamma(n)\Gamma(1+\frac{k}{2})}{\Gamma(L+\frac{k}{2})}(1-\mu^2)^n\,{}_3F_2\left(1+\frac{k}{2},n,n;n+\frac{k}{2},1;\mu\right) \tag{21}$$

where ${}_pF_q$ is the generalised hypergeometric function and $\Gamma(\cdot)$ is the gamma function. The first moment, bias, and second moment are shown in Figures 4a, 4b and 4c respectively, for $\{n \in [60, 120, 180]\}$. The bias is largest for small n and low μ.

A. Non-Zero Lag Bias

The non-zero lag coherence bias can be minimized by performing a time delay and RPC yaw compensation prior to estimation of the coherence. We begin the process with range-windowed signals $s_{a,p,q}[t]$ from (1), calculate the normalised cross-correlation function for all relevant phase centre pairs using (5), and take the maximum over a subset of temporal lags using (9) to populate $\hat{\boldsymbol{\rho}}_q$. Taking the mean across the diagonals of the upper triangle of $\hat{\boldsymbol{\rho}}_q$ using (10) and finding the index of the maximum value gives an estimate of the integer number of overlapping phase centres $\hat{\eta}$. We then form the matrix of normalised cross-correlations for these maximally overlapping phase centres by introducing the RPC array axis

$$u = \left[-\frac{\hat{\eta}-1}{2},\ldots,\frac{\hat{\eta}-1}{2}\right]\frac{\Delta}{2} \tag{22}$$

and re-indexing of the result of (5) to extract the normalised cross-correlation functions of the maximally overlapping phase centre pairs as a function of RPC array axis u and temporal lag τ.

$$\hat{\upsilon}[u_b,\tau] = \hat{\rho}_{a',b}[\tau], \tag{23}$$

where $a' = A-(\hat{\eta}-b)$ and $\{b \in [1,...,\hat{\eta}]\}$. This matrix of normalised cross-correlations is then beamsteered [24] over a range of angles ϕ by

$$\hat{\Upsilon}[\phi,\tau] = \sum_u \hat{\upsilon}[u,\tau]\exp(jk_c u\sin(\phi)) \tag{24}$$

where $k_c = 2\pi f_c/c$ is the wavenumber at centre frequency f_c. The location

$$(\hat{\phi}',\hat{\tau}') = \underset{\phi,\tau}{\arg\max}\left\{\left|\hat{\Upsilon}\left[\phi,\tau\right]\right|\right\} \tag{25}$$

gives a sample-precision estimate of the time delay $\hat{\tau}'$ between the signals, and an estimate of the RPC yaw $\hat{\phi}'$, which is refined using the Lagrange three-point quadratic interpolation formula [18] to give $\hat{\phi}$. The time delay

[2]The Gauss hypergeometric function is challenging to compute for large n. We use the variable-precision floating-point arithmetic (VPA) capability in MATLAB to compute (20).

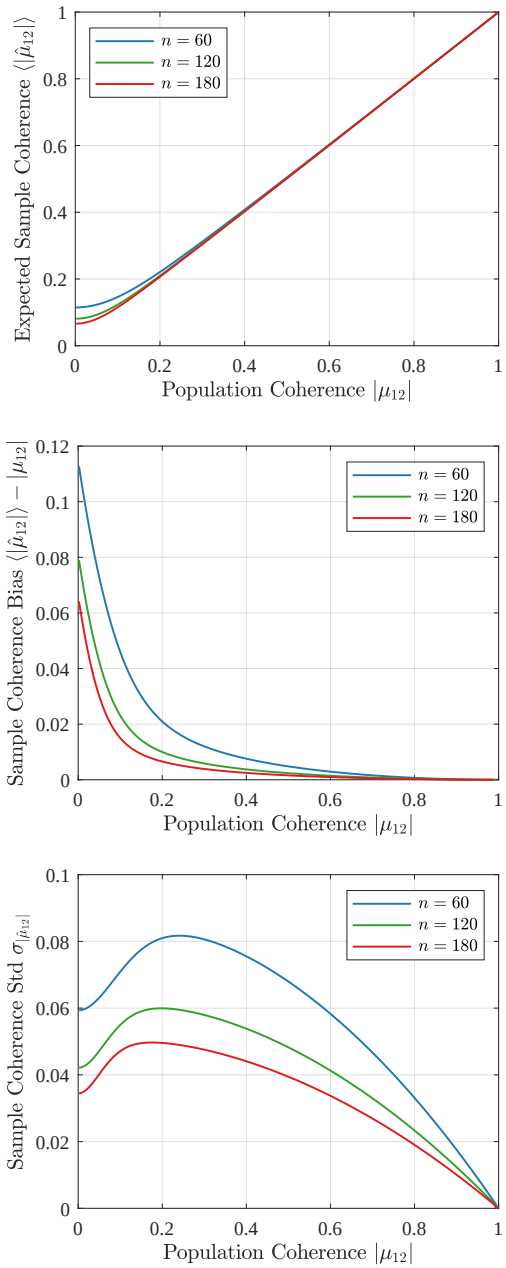

Fig. 4: Statistics of the sample coherence $\hat{\mu}_{12}$ between complex baseband signals. (a) The expected value of sample coherence $\hat{\mu}_{12}$, showing significant bias for low values of population coherence μ_{12}. (b) The bias and (c) standard deviation of the sample coherence estimate.

estimates are refined by exploiting the phase of the peak coherence using the process in [25] to give the fine time delay estimate $\hat{\tau}$. A possible improvement to this process is to use a sinus cardinal model to refine the time delay estimate instead of quadratic interpolation, which has been demonstrated to reduce time delay estimation bias [26].

Once estimates for the fine time delay $\hat{\tau}_q$ and RPC yaw $\hat{\phi}_q$ have been made, the data are re-windowed such that

$$s'_{a,p_1,q}[t] = s_{a,p_1}[t] \operatorname{rect}\left(\frac{t - t_q}{\tau}\right) \tag{26}$$

as before, and

$$s'_{b,p_2,q}[t] = s'_{b,p_2,q}\left[t - \left(\frac{u_b \sin\left(\hat{\phi}_q\right)}{c} - \hat{\tau}_q\right)\right] \operatorname{rect}\left(\frac{t - t_q}{\tau}\right). \tag{27}$$

which temporally aligns the redundant signals. We can now form the matrix of coherence estimates $\hat{\boldsymbol{\mu}}_q$ using the normalised zero-lag cross-correlation function (4). This matrix of coherence estimates is now assumed to be only affected by the zero-lag coherence bias.

B. Zero Lag Bias

The temporal registration in Section III-A serves to remove the non-zero lag coherence bias. However, the zero-lag coherence bias remains and must be compensated in order to reduce along-track micronavigation bias. While it can be shown that no unbiased estimator of sample coherence exists, there are strategies that can mitigate the remaining zero-lag coherence bias [11]. Since the probability density function (PDF) of the sample coherence as computed by the zero-lag normalised cross-correlation is known under the assumption of jointly complex circular Gaussian distributed signals, we now take a Bayesian approach to reducing the coherence estimation bias.

We begin with the matrix of sample coherences $\hat{\boldsymbol{\mu}}_q$. The values along the diagonals of $\hat{\boldsymbol{\mu}}_q$ are redundant and potentially correlated sample estimates of spatial coherence at the same spatial lag. The correlation between the covariances from which these sample spatial coherence estimates are derived can be predicted given the geometry and the sonar parameters [27, Eq. (8)]. For geometries and sonar parameters that result in sufficiently low correlation between adjacent sample spatial coherence estimates, we can approximate these estimates as independent and perform a Bayesian estimation [28], [29] of the underlying population coherence from these samples using the rectangular prior

$$p(\mu) = \begin{cases} 1 & \text{if } 0 < \mu \leq 1 \\ 0 & \text{otherwise} \end{cases} \tag{28}$$

by the following process. The posterior distribution for the population coherence for each candidate overlap η is given by the product of the posterior distributions over all samples along the diagonal of $\hat{\boldsymbol{\mu}}_q$ corresponding to the candidate overlap η

$$\mathrm{P}(\mu_\eta; \hat{\mu}, n) = \prod_{b=1}^{\eta} \left\{ \frac{\mathrm{P}(\hat{\mu}_{a',b}; \mu, n) p(\mu)}{\int \mathrm{P}(\hat{\mu}_{a',b}; \mu, n) p(\mu) d\mu} \right\}, \tag{29}$$

where $a' = A - b + 1$ and the product is computed using a sum of log posterior functions to avoid numerical errors. The Bayes coherence estimate is computed by

$$\bar{\mu}[\eta] = \int \mu \, \mathrm{P}(\mu_\eta; \hat{\mu}, n) d\mu, \tag{30}$$

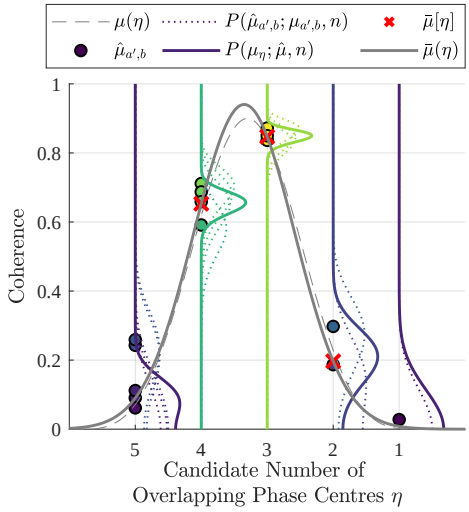

Fig. 5: The process of estimating the sub-sample number of overlapping phase centres using Bayesian coherence estimation. The dashed line represents the underlying spatial coherence $\mu(\eta)$. The filled dots show the same sample coherence estimates as Figure 1b. Each of these samples has a likelihood shown by dotted lines $\mathrm{P}(\hat{\mu}_{a',b};\mu_{a',b},n)$, and (29) gives the product of these likelihoods (multiplied by the prior and normalised), giving the overall posteriors $\mathrm{P}(\mu_\eta;\hat{\mu},n)$ which are plotted as solid lines. The likelihood and posterior distributions at each spatial lag have been scaled for clarity of display.The expected value of the posterior gives the expected population coherence $\bar{\mu}[\eta]$. Finally, an interpolation kernel is fitted to the three red crosses representing the peak Bayes coherence estimate and the adjacent samples, to give an estimate $\bar{\mu}(\eta)$ of the underlying coherence function.

which is the expected value of the posterior distribution. An interpolation kernel can then be fitted to the largest coherence estimate and its adjacent samples, allowing an estimate of the location of the peak underlying coherence to be made. The process of Bayesian coherence estimation and subsequent interpolation is shown in Figure 5.

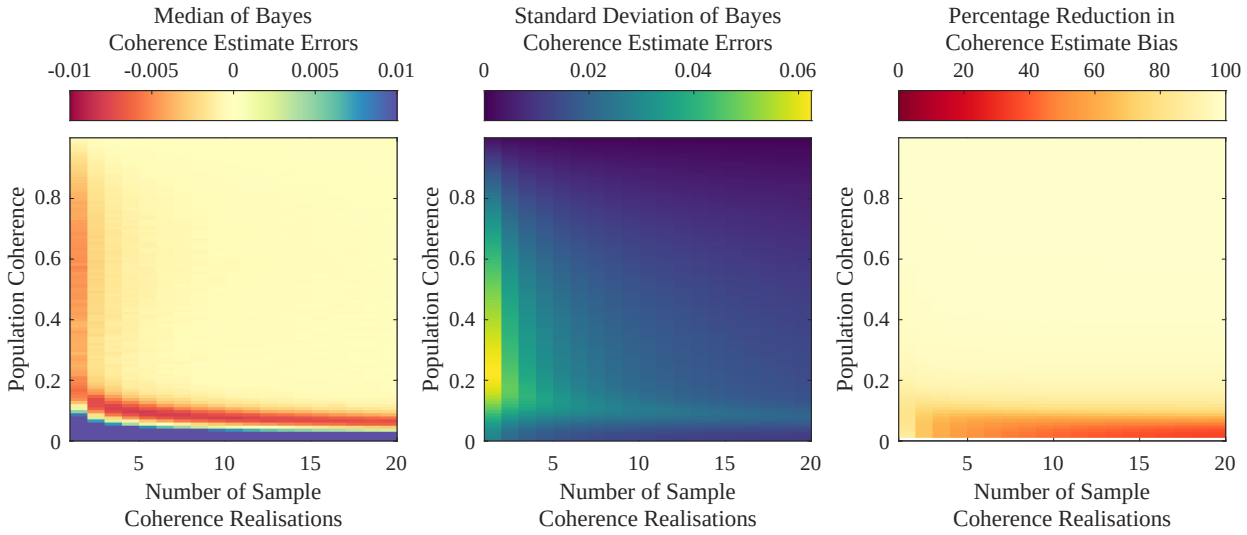

Fig. 6: Statistics of Bayesian coherence error removal, for signals with $n = 120$ independent samples. (a) Median of Bayes coherence estimates, showing that the Bayes estimate is asymptotically unbiased. (b) Standard deviation of Bayes coherence estimates. (c) The percentage reduction in coherence estimate bias achieved by the Bayesian estimation method.

While Bayes estimators are in general asymptotically unbiased, they are not necessarily unbiased for a finite number of samples. The performance of the Bayes coherence estimator is demonstrated in Figure 6, which shows the bias and standard deviation of the Bayes coherence estimate as a function of population coherence and number of sample coherence realisations from a Monte Carlo simulation. This shows that both the residual bias and standard deviation of the the Bayes coherence estimate are reduced for larger numbers of sample coherence realisations, as expected for an asymptotically unbiased estimator. Extremely low residual bias is seen for most values of population coherence and number of sample coherence realisations, and over 90% bias reduction is achieved for all population coherence values above 0.175.

IV. Improved Coherence Estimation Interpolation Kernel

The van Cittert-Zernike theorem for a narrowband pulsed active sonar system derived by Brown [12] gives the zero-lag covariance of the field as

$$\gamma_{12} \propto \int_{\Psi} \beta_1(\boldsymbol{\chi})\beta_2(\boldsymbol{\chi})\sigma(\boldsymbol{\chi})\Lambda\left(\boldsymbol{\chi}, \frac{t_2 - t_1}{2}, t_2 - t_1\right) e^{jk(R_1 - R_2)} d\boldsymbol{\chi}, \tag{31}$$

where the geometry is defined by Figure 7, t_1 and t_2 define the temporal interval over which the covariance is calculated, $\boldsymbol{\chi}$ represents a point in the integration volume Ψ and

$$R_m = \|\boldsymbol{\chi}_{\mathrm{t}_m} - \boldsymbol{\chi}\| + \|\boldsymbol{\chi}_{\mathrm{r}_m} - \boldsymbol{\chi}\| \,, \quad m \in 1, 2 \tag{32}$$

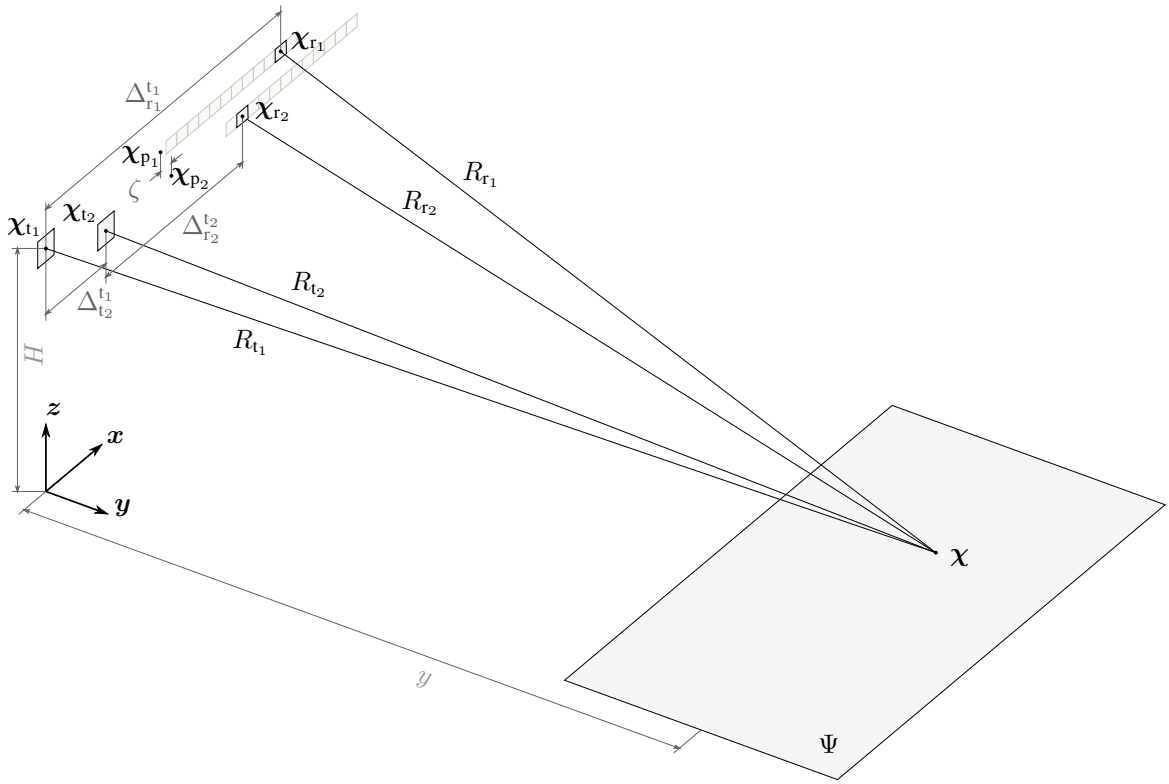

Fig. 7: Geometry for the evaluation of (31) and (36), showing two successive pings. The acoustic field is transmitted from positions $\boldsymbol{\chi}_{\mathrm{t}_1}$and $\boldsymbol{\chi}_{\mathrm{t}_2}$, scattered by the region Ψ, and received at receiver positions $\boldsymbol{\chi}_{\mathrm{r}_1}$and $\boldsymbol{\chi}_{\mathrm{r}_2}$. The two highlighted receivers are selected to form the spatial coherence function in Figure 9a. The transducer arrays are shown offset vertically for clarity.

gives the two-way propagation distances for successive pings indexed by m. The transducer directivity functions and spreading loss are gathered in the terms

$$\beta_m(\boldsymbol{\chi}) = \alpha\, b_{\mathrm{TX}}(\boldsymbol{\chi})\, b_{\mathrm{RX}}(\boldsymbol{\chi}) \tag{33}$$

where b_{TX} and b_{RX} are the transmitter and receiver directivity functions respectively and

$$\alpha = \frac{1}{2\pi \left(\frac{R_m}{2}\right)^2} \tag{34}$$

models spherical spreading loss. $\sigma(\boldsymbol{\chi}) = \sigma_0(\boldsymbol{\chi})\xi(\boldsymbol{\chi})$ is the spatially dependent scattering strength, which combines the bottom scattering strength projected onto the seafloor $\sigma_0(\boldsymbol{\chi})$ and a multiplicative loss term $\xi(\boldsymbol{\chi})$. The masking function Λ confines the contributions to a finite volume on the seafloor via the function

$$\Lambda(\boldsymbol{\chi}, t, \tau) = \begin{cases} 0, \text{ if } \frac{1}{\tau}\left|t - \frac{2}{c}\left|\boldsymbol{\chi} - \boldsymbol{\chi}_{\mathrm{t}_1}\right|\right| > \frac{1}{2} \\ \frac{1}{2}, \text{ if } \frac{1}{\tau}\left|t - \frac{2}{c}\left|\boldsymbol{\chi} - \boldsymbol{\chi}_{\mathrm{t}_1}\right|\right| = \frac{1}{2} \\ 1, \text{ if } \frac{1}{\tau}\left|t - \frac{2}{c}\left|\boldsymbol{\chi} - \boldsymbol{\chi}_{\mathrm{t}_1}\right|\right| < \frac{1}{2} \end{cases} \tag{35}$$

where c is the sound speed and τ is the temporal window length. The zero-lag covariance may be normalised to give the correlation coefficient, using

$$\mu_{12}(t_1, t_2) = \frac{\gamma_{12}(t_1, t_2)}{\sqrt{\gamma_{11}(t_1, t_2)\gamma_{22}(t_1, t_2)}}. \tag{36}$$

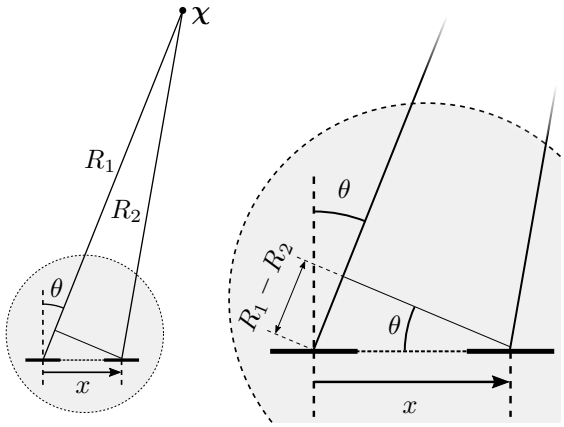

Fig. 8: The geometry of a phase centre advancing in the along-track x direction, showing the approximation for the range difference $R_1 - R_2$ given in (41) for a point $\boldsymbol{\chi}$ at an angle θ from broadside.

Evaluating (31) and (36) allows the spatial coherence of the acoustic field to be predicted. Here, we seek a range-independent analytical approximation for the spatial coherence as a function of along-track motion between successive pings to use as an interpolation kernel. Making an assumption of constant variance $\gamma_{11}(t_1, t_2)$ and $\gamma_{22}(t_1, t_2)$ over the relevant domain of x, (36) reduces to

$$\mu_{12}(t_1, t_2) \propto \gamma_{12}(t_1, t_2). \tag{37}$$

The approximation of range independence is achieved by approximating the spreading loss α as a constant across the temporal window, and by neglecting the temporal masking function Λ. Making a further assumption of spatially constant seafloor scattering strength $\sigma(\boldsymbol{\chi})$ and constraining the sensor motion to the along-track direction we arrive at the expression

$$\mu_{12}(x) \propto \int_{\Psi} \left(b_{\text{TX}}\left(\boldsymbol{\chi}\right) b_{\text{RX}}\left(\boldsymbol{\chi}\right)\right)^2 e^{jk(R_1 - R_2)} d\boldsymbol{\chi}. \tag{38}$$

In the far field, the phase centre approximation [30] can be used, which is applicable in this context when

$$\frac{L^2}{4R}\left(1 - \cos^2\left(\frac{\theta_{3\text{dB}}}{2}\right)\right) \ll 1 \tag{39}$$

where L is the largest distance between the transmit and receive transducers, R is range and $\theta_{3\,\text{dB}}$ is the $3\,\text{dB}$ width of the transmission beampattern. Combining this with a far-field approximation, valid in the Fraunhoffer region,

$$R > \frac{2x^2}{\lambda}, \tag{40}$$

the difference in range from a point to two phase centres can be approximated as

$$R_1 - R_2 \approx x \sin(\theta), \tag{41}$$

as shown in Figure 8, where $\theta = f(\boldsymbol{\chi})$ is the angle from broadside and x is the along-track displacement between phase centres. For the design of rectangular transmit and receive transducers, we arrive at

$$\mu_{12}(x) \propto \int_{\Psi} \operatorname{sinc}\left(kL_{\text{TX}} \sin(\theta)\right)^2 \operatorname{sinc}\left(kL_{\text{RX}} \sin(\theta)\right)^2 e^{jk\sin(\theta)x} d\boldsymbol{\chi}, \tag{42}$$

where L_{TX} and L_{RX} are the along-track lengths of the transmitter and receiver respectively. This can be interpreted as the Fourier transform of the combined transducer beampattern squared, which, by the convolution theorem, is the convolution of the squared transducer shading functions. For rectangular shading (i.e. sinc beampatterns) this is equivalent to the convolution of two triangular functions, resulting in a cubic function. For a system with $L_{\text{TX}} = \kappa L_{\text{RX}}$, (42) has been evaluated using the Wolfram Engine [31] as

$$\begin{aligned}\mu_{12}(x) = \mu_0 \Big(&- 2\left|x - 2\kappa L_{\text{RX}}\right|^3 + \left|x + (2-2\kappa)L_{\text{RX}}\right|^3 + \left|x + (-2-2\kappa)L_{\text{RX}}\right|^3 - 2\left|x + 2L_{\text{RX}}\right|^3 + 4\left|x\right|^3 \\ &- 2\left|x - 2L_{\text{RX}}\right|^3 + \left|x + (2+2\kappa)L_{\text{RX}}\right|^3 + \left|x + (-2+2\kappa)L_{\text{RX}}\right|^3 - 2\left|x + 2\kappa L_{\text{RX}}\right|^3 \Big)\end{aligned} \tag{43}$$

and for the design choice of $\kappa = 1.5$ (e.g. [32]) such that the first null of the transmitter beampattern coincides with the peak of the first sidelobe of the receiver beampattern, this results in the series [33]

$$\mu_{12}(x) \propto \sum_{i=0}^{10} h_i |x - (i-5)L_{\text{RX}}|^3, \tag{44}$$

where $h = [1, 0, -2, -2, 1, 4, 1, -2, -2, 0, 1]$.

An improved interpolation kernel can be formulated based on (43) or (44) by replacing x with $x - \zeta$ and L_{RX} with w, where ζ is the peak offset and w is the kernel width. We refer to this as the *cubic* kernel. We consider a system with $\kappa = 1.5$ in the following and the resulting interpolation kernel takes the form

$$\mu(x) = \mu_0 \sum_{i=0}^{10} h_i \left|x - \zeta - (i-5)w\right|^3 \tag{45}$$

where μ_0 is the peak coherence and w is the kernel width. In the following section we compare this to the Gaussian interpolation kernel proposed in [14], which takes the form

$$\mu(x) = \mu_0 \exp\left\{-\frac{1}{2}\frac{(x-\zeta)^2}{\sigma^2}\right\} \tag{46}$$

where σ defines the kernel width.

A. Interpolation Kernel Comparison

The quality of fit of the Gaussian and cubic interpolation kernels is now compared to the spatial coherence function predicted by (36). We consider specific elements of a SAS with a receiving array consisting of 12 elements performing two successive pings, operating with centre frequency $f_c = 300\,\text{kHz}$, bandwidth $B = 60\,\text{kHz}$, sound speed $c = 1500\,\text{m/s}$, transmitter and receiver lengths $L_{\text{TX}} = 50\,\text{mm}$ and $L_{\text{RX}} = 33\,\text{mm}$ respectively, and altitude $H = 10\,\text{m}$. The geometry of the SAS closely mimics the Minehunting UUV for Shallow water Covert Littoral

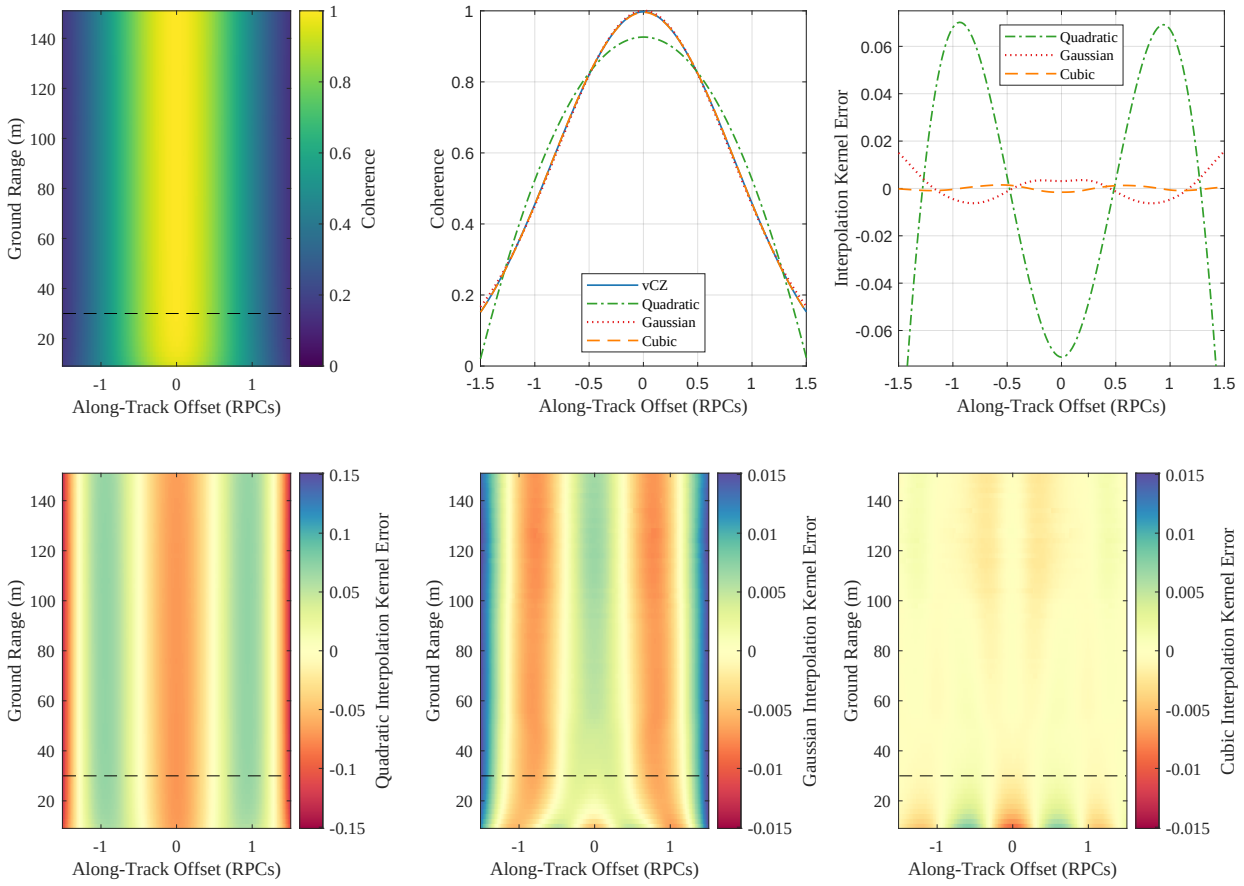

Fig. 9: (a) The spatial coherence function predicted by (36), as a function of ground range, for system parameters matching those of the MUSCLE SAS. (b) A slice through (a) at $y = 30\,\mathrm{m}$, with the best-fitting quadratic, Gaussian and cubic kernels for comparison. (c) The error between the van Cittert-Zernike simulation and the best-fitting quadratic, Gaussian and cubic kernels. (d,e,f) The fit error for the quadratic, Gaussian and cubic interpolation kernels respectively. Note the colour axis is compressed by a factor of 10 in (e,f) compared to (d).

Expeditions (MUSCLE) SAS [32] operating in interferometric mode with a receiver array of 12 elements spaced at $\Delta = 33\,\mathrm{mm}$ and an along-track advance between pings of

$$\Delta_{\mathrm{t}_2}^{\mathrm{t}_1} = (9 + \zeta)\,\frac{\Delta}{2}, \tag{47}$$

where ζ is the along-track offset in phase centres between the phase centre arrays formed by the foremost and aftmost 3 phase centres of adjacent pings. The along-track distance between the transmitter and the 'fore' phase centre array is $\Delta_{\mathrm{r}_1}^{\mathrm{t}_1} = 850\,\mathrm{mm}$ and between the transmitter and the 'aft' phase centre array is $\Delta_{\mathrm{r}_2}^{\mathrm{t}_2} = 553\,\mathrm{mm}$, as shown in Figure 7.

We evaluate (31) and (36) for an infinite horizontal plane over the domain $-1.5 \leq \zeta \leq 1.5$, which is the range of phase centre offsets over which samples are drawn to fit the interpolation kernel, and $10\,\mathrm{m} \leq y \leq 150\,\mathrm{m}$, which

is a reasonable swath for a modern SAS. The beampatterns β_m are evaluated for unshaded rectangular apertures, the scattering strength $\sigma(\boldsymbol{\chi})$ is assumed to be constant over each temporal window, and the temporal limits for the masking function are given by

$$t_1 = 2\frac{\sqrt{y^2+H^2}}{c} - \frac{n}{2B} \tag{48}$$

$$t_2 = 2\frac{\sqrt{y^2+H^2}}{c} + \frac{n}{2B}, \tag{49}$$

where the number of independent samples in the temporal window $n = 120$, which corresponds to a spatial window length of $1.5\,\mathrm{m}$. This results in the spatial coherence function $\mu_{1,2}(x,y)$ shown in Figure 9a.

At each value of ground range y_i, we now fit the Gaussian kernel (46) by performing the least-squares minimisation

$$[\hat{\mu}_0, \hat{\sigma}, \hat{\zeta}] = \arg\min \left\{ \sum_x \left(\mu_0 \exp\left\{ -\frac{1}{2}\frac{(x-\zeta)^2}{\sigma^2} \right\} - \mu_{12}(x,y) \right)^2 \right\} \tag{50}$$

and finding the fit error as a function of RPC offset using

$$\epsilon_{\mathrm{g}}(x,y) = \hat{\mu}_0 \exp\left\{ -\frac{1}{2}\frac{(x-\hat{\zeta})^2}{\hat{\sigma}^2} \right\} - \mu_{12}(x,y), \tag{51}$$

which is shown in Figure 9e. We perform the same procedure for the cubic kernel, finding the optimal parameter values by the least-squares minimisation

$$[\hat{\mu}_0, \hat{w}, \hat{\zeta}] = \arg\min \left\{ \sum_x \left(\mu_0 \sum_{i=0}^{10} h_i \left| x - \zeta - (i-5)w \right|^3 - \mu_{12}(x,y) \right)^2 \right\}, \tag{52}$$

and finding the fit error by

$$\epsilon_{\mathrm{v}}(x,y) = \hat{\mu}_0 \sum_{i=0}^{10} h_i |x - \hat{\zeta} - (i-5)\hat{w}|^3 - \mu_{12}(x,y), \tag{53}$$

which is shown in Figure 9f. This indicates that the cubic kernel offers a significantly improved fit compared to the Gaussian kernel. Figure 9 also includes equivalent results from a quadratic kernel, for consistency and comparison with Fig. 4 of [14].

V. Simulation Results

The effect of the along-track micronavigation bias reduction methods presented in Sections III and IV is now demonstrated using two independent Monte Carlo simulation methods. Section V-A describes the use of these simulations to quantify the expected bias and standard deviation of along-track micronavigation estimates as a function of the number of overlapping phase centres, using all combinations of the bias reduction methods. Having quantified these biases and standard deviations, we then evaluate the navigation error as a function of distance travelled for a set of random walks covering a variety of possible operating characteristics in Section V-B.

The first simulation method involves using the van Cittert-Zernike theorem to predict the population coherence between phase centre pairs, and simulating biased coherence samples by randomly drawing samples from the probability distribution for sample coherence given by (20). These simulations allow investigation of the effect of Bayesian coherence estimation and the improved interpolation kernel. However, since this simulation directly

simulates coherence under the assumption that the redundant signals are perfectly temporally registered, the effect of the temporal registration method is not investigated. Therefore, a point-scatterer simulation similar in type to [34] has also been used which generates simulated echo data for a given geometry. While this simulation method is more realistic, it is still highly idealised, with a perfectly linear vehicle trajectory at an altitude of $10\,\mathrm{m}$ above a flat, horizontal seafloor. The geometry of the SAS used in both simulations closely replicates that of the MUSCLE system operating in interferometric mode, as in Section IV-A. This geometry results in a correlation between adjacent sample covariance estimates (those from which the elements of the matrix of sample coherences $\hat{\boldsymbol{\mu}}_q$ are derived) of 0.18, which we consider to be sufficiently small to allow coherence estimates from adjacent phase centre pairs to be approximated as independent. The seafloor is represented by a collection of in-plane point-scatterers, where each ideal resolution cell contains a number of randomly distributed points drawn from a negative binomial distribution [35] with mean 10 and success probability 0.5. The beampatterns for each transducer are calculated at the centre frequency of $300\,\mathrm{kHz}$ assuming rectangular apertures with no shading. The effect of spreading loss is not modelled, since practical SAS systems typically apply a range-varying gain on reception, and the change in signal-to-noise ratio (SNR) over individual temporal windows is expected to be negligible. After summing the beampattern-weighted response over all scatterers, the SNR is reduced to $30\,\mathrm{dB}$ using additive white Gaussian noise. Using the point-scatterer simulation allows the full processing chain to be implemented from received echo signals through to along-track micronavigation estimates. Using this simulation method, the effect of temporal registration, Bayesian coherence estimation and the improved interpolation kernel can all be investigated and quantified.

A. Bias and standard deviation of along-track micronavigation estimates

Figure 10 shows the median and standard deviation of the along-track micronavigation estimates for both simulation methods. Consider first Figure 10a, which shows the median advance per ping error for a range of true advances, shown as the number of overlapping phase centres per ping. Using all of the potential combinations of methods, a periodic error is seen that repeats every integer number of overlapping phase centres, which crosses its median value at every multiple of 0.5 phase centres.

The results derived from the point scatterer simulation without temporal registration reveals an offset in median error that is approximately constant as a function of the number of overlapping phase centres. The median error without temporal registration varies around approximately 0.003 phase centre spacings, but with the temporal registration this offset is virtually eliminated. Furthermore, the median errors resulting from the point simulation with temporal registration show close correspondence with those from the van Cittert-Zernike simulation.

We now consider the impact of Bayesian coherence estimation and the choice of interpolation kernel. Consider first the median error using the Gaussian kernel. The Bayes coherence estimator increases the maximum absolute error by over 50%. This suggests that the Gaussian interpolation kernel is a better fit to the biased sample coherences than those with the coherence bias compensated for. Using the empirically derived cubic kernel with the conventional estimator results in a modest reduction in maximum absolute error of around 20% compared to the standard estimator with the Gaussian kernel, which is considered to be the current gold standard. However, using the Bayes estimator and the cubic kernel improves this further, with a reduction in maximum absolute error of up to 80%.

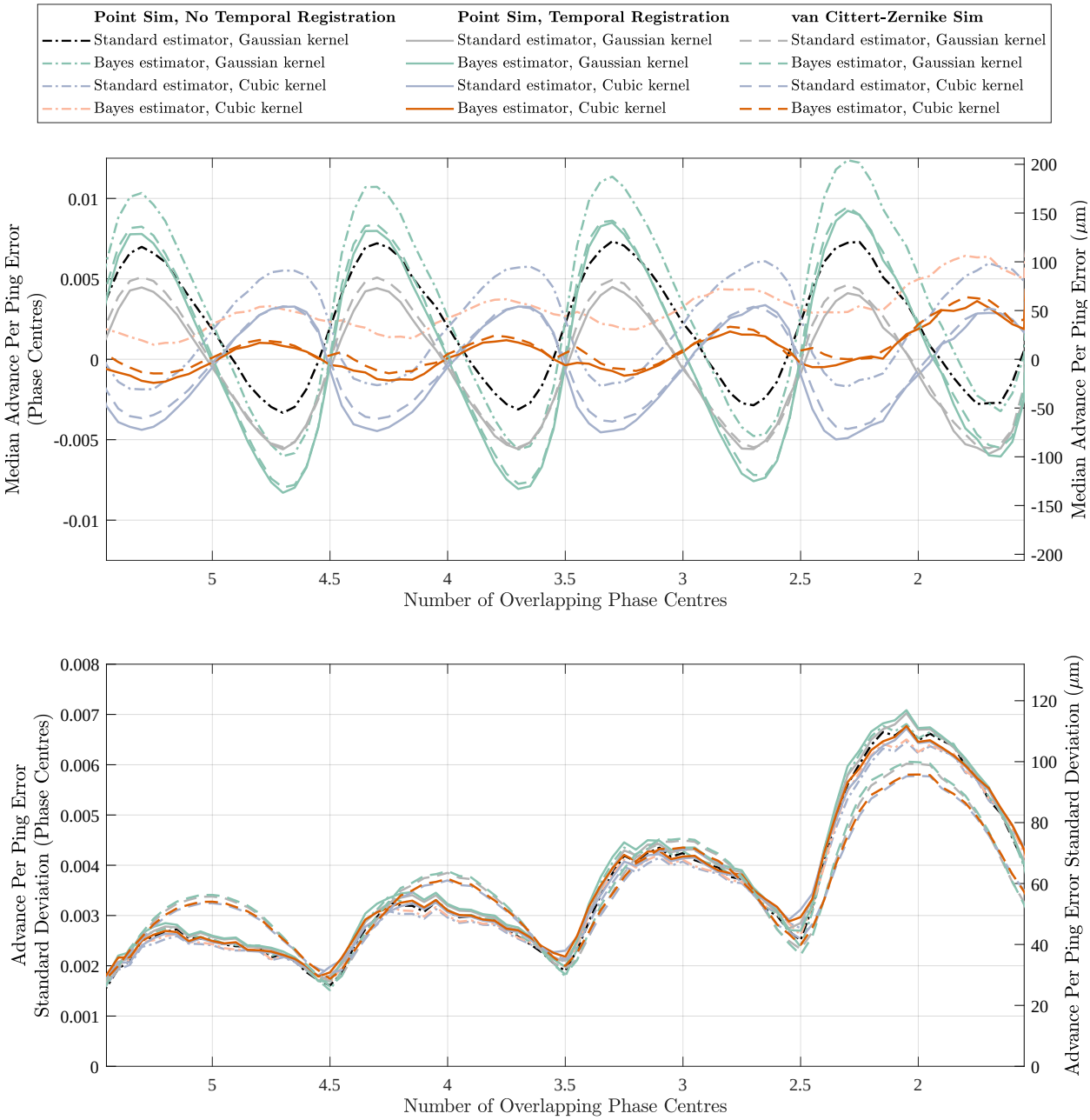

Fig. 10: (a) The median and (b) standard deviation of the along-track micronavigation estimate from both the point simulation and the van Cittert-Zernike simulations. The 'standard' estimator refers to taking the mean coherence over diagonals of the matrix of individual coherence estimates as in (10), rather than the Bayesian approach of (29).

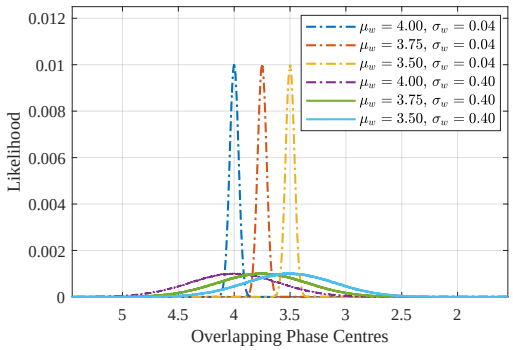

Fig. 11: The distribution of the number of overlapping phase centres for the 6 random walks considered.

This improvement is most significant with a larger number of overlapping phase centres per ping. This is expected because more overlapping phase centres results in more coherence samples in the Bayes estimator. The reduced residual bias with more independent samples is demonstrated in Figure 6a.

The standard deviation of the error is shown in Figure 10b, which shows good correspondence between the simulation methods. The error standard deviation is reduced in all cases with more overlapping phase centres between pings and when the phase centres are half overlapping in all cases. The standard deviation of the advance per ping error is similar for all of the bias reduction methods. However, there is a noticeable disparity between the simulated error standard deviation derived from the point simulator and the van Cittert-Zernike simulator.. This is likely to be because the Monte Carlo draws from (20) are independent, but the sample coherences estimated between adjacent phase centre pairs are correlated with correlation coefficient 0.18. Additionally, the random distribution of point-scatterers may not result in perfectly zero-mean circular Gaussian distributed signals. Nevertheless, the error standard deviation follows a similar pattern for both simulators, with reducing standard deviation with more overlap between pings. This is to be expected, since more redundant data is available when there is greater overlap between pings. Overlaid on this trend is a variation in standard deviation with local minima occurring at the locations of maximal phase centre misalignment (4.5, 3.5, 2.5 overlapping phase centres).

The implication of Figure 10 is that along-track micronavigation bias can be reduced by adjusting the vehicle speed or ping rate such that the number of overlapping phase centres is a multiple of 0.5. Furthermore, the standard deviation of along-track micronavigation estimates can be reduced when phase centres are maximally misaligned. In the following, we investigate the attainable along-track navigation performance for SAS systems by simulating the along-track micronavigation error as a function of distance travelled for a range of operating conditions.

B. Micronavigation error evaluation using random walks

In this section, we consider the accumulation of along-track navigation error as a function of distance travelled, for a range of possible operating scenarios. We do so by simulating 1×10^6 Monte Carlo uncorrelated random walks of $1000\,\mathrm{m}$ in length, where the number of overlapping phase centres between each ping pair is drawn from a Gaussian distribution with mean μ_w and standard deviation σ_w. The error introduced on each ping pair is drawn

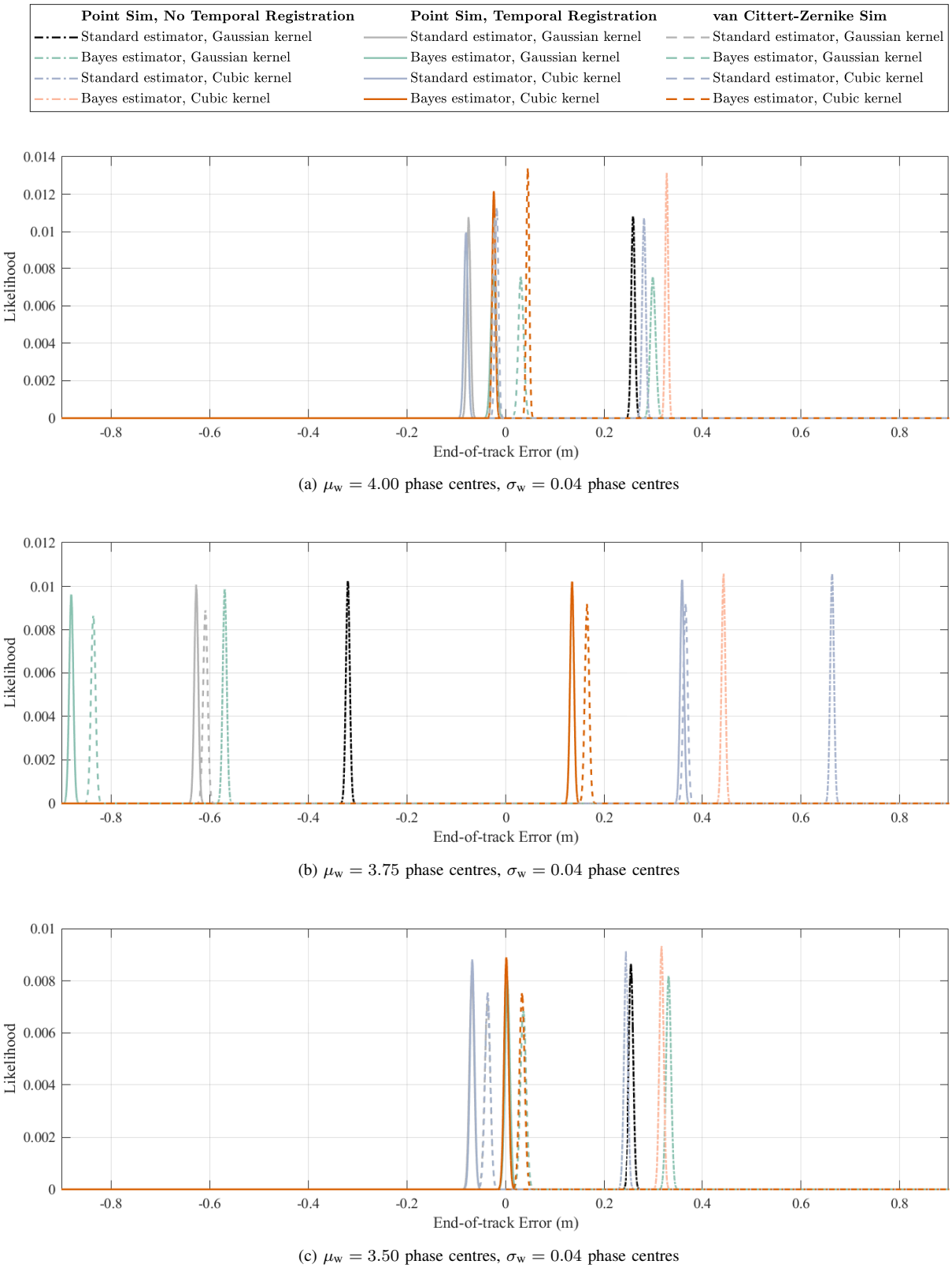

(a) $\mu_{\mathrm{w}} = 4.00$ phase centres, $\sigma_{\mathrm{w}} = 0.04$ phase centres

(b) $\mu_{\mathrm{w}} = 3.75$ phase centres, $\sigma_{\mathrm{w}} = 0.04$ phase centres

(c) $\mu_{\mathrm{w}} = 3.50$ phase centres, $\sigma_{\mathrm{w}} = 0.04$ phase centres

Fig. 12: End-of-track error distributions after $1000\,\mathrm{m}$ random walks, for systems with 1% variability in overlapping phase centres between adjacent pings.

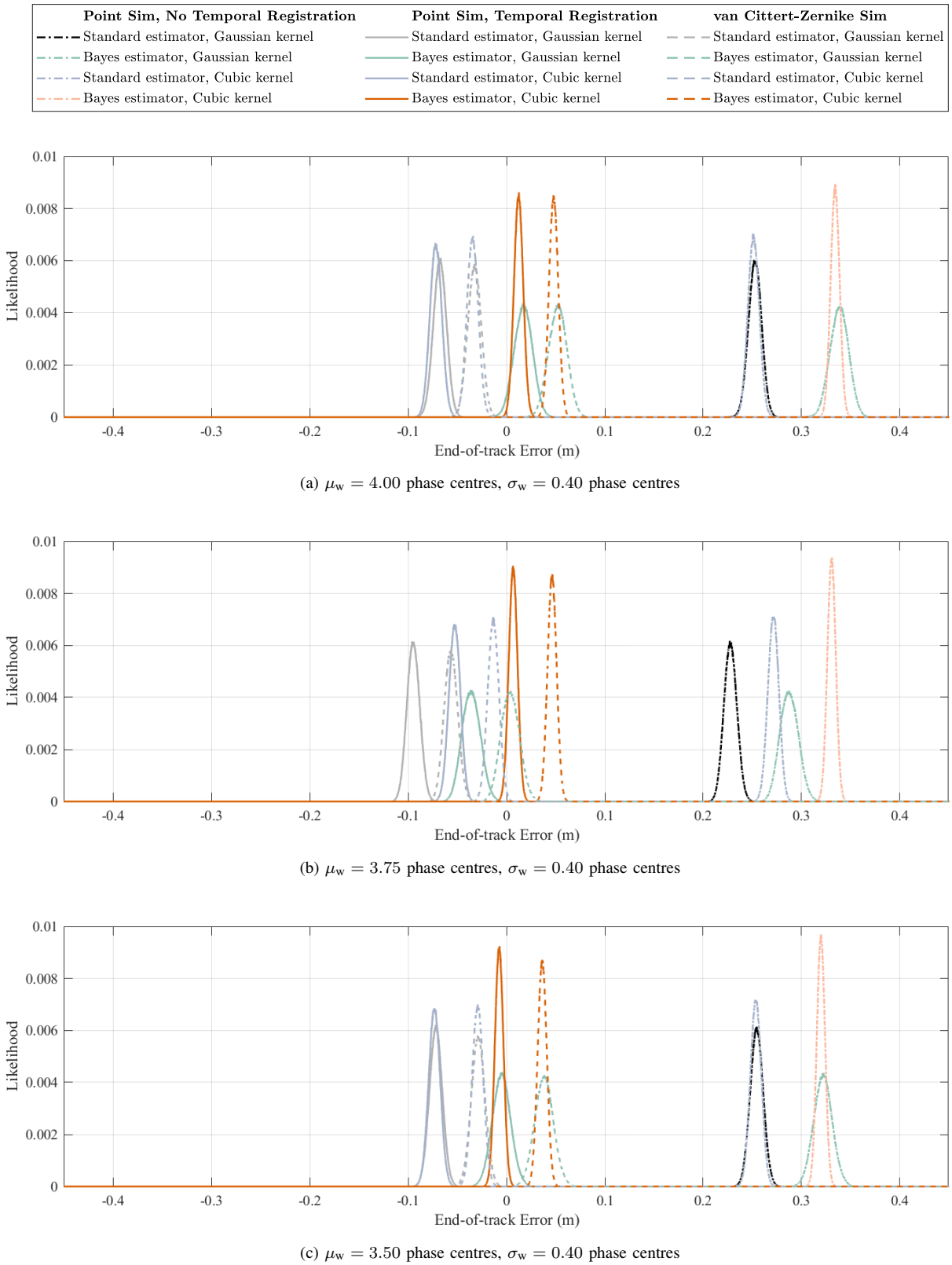

(a) $\mu_{\mathrm{w}} = 4.00$ phase centres, $\sigma_{\mathrm{w}} = 0.40$ phase centres

(b) $\mu_{\mathrm{w}} = 3.75$ phase centres, $\sigma_{\mathrm{w}} = 0.40$ phase centres

(c) $\mu_{\mathrm{w}} = 3.50$ phase centres, $\sigma_{\mathrm{w}} = 0.40$ phase centres

Fig. 13: End-of-track error distributions after $1000\,\mathrm{m}$ random walks, for systems with 10% variability in overlapping phase centres between adjacent pings.

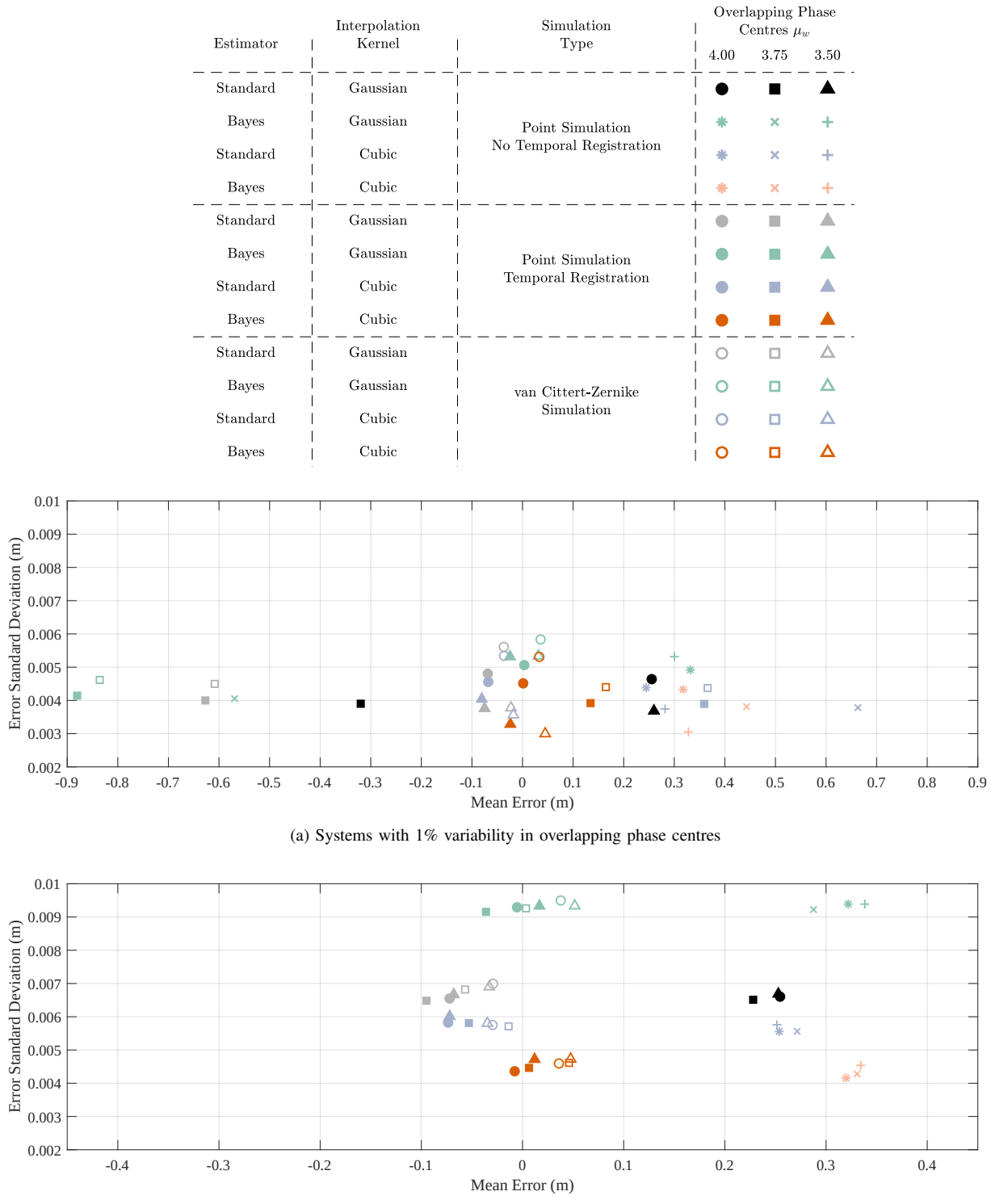

(a) Systems with 1% variability in overlapping phase centres

(b) System with 10% variability in the number of overlapping phase centres (Note mean error axis is dilated by a factor of 2 compared to (a))

Fig. 14: Summary of the mean and standard deviation of the end-of-track errors for selected values of the mean μ_{w} and standard deviation σ_{w} of the true number of overlapping phase centres between pings.

from the distributions shown in Figure 10. We investigate two cases for the standard deviation of the distribution, representing low and high variability in the number of overlapping phase centres. Considering a nominal inter-ping overlap of 4 phase centres, $\sigma_{\mathrm{w}} = 0.04$ phase centres and $\sigma_{\mathrm{w}} = 0.4$ phase centres represent standard deviations of 1% and 10% respectively. The low variability distribution may be representative of SAS systems operating with variable ping rate, where the inter-ping overlap is controlled by altering the ping rate as a function of along-track velocity measured by an onboard sensor such as a DVL. The high variability distribution may represent SAS systems with a constant ping rate, with the along-track velocity of the platform controlled with the goal of achieving μ_{w} overlapping phase centres. The three values of $\{\mu_{\mathrm{w}} \in [4.00, 3.75, 3.50]\}$ phase centres are used for both of these system types. These parameters are chosen to represent maximal phase centre overlap (a common choice in practice), a likely worst case scenario resulting from potential errors in ping rate control or vehicle velocity control, and maximal misalignment of phase centres in order to minimise the error standard deviation and bias as proposed in Section V-A.

Figures 12 and 13 show the distribution of end-of-track error for each random walk, with along-track motion estimated by each possible combination of the presented bias reduction methods, for the variable and constant ping rate cases respectively. These figures are summarised in Figure 14, where the means and standard deviations of the end-of-track errors are plotted. The black lines and markers denote the current gold standard method, which does not include temporal registration or Bayesian coherence estimation, and uses a Gaussian interpolation kernel. The orange lines and markers denote the proposed method, with temporal registration, Bayesian coherence estimation and the cubic interpolation kernel. Consider the results for low variability in inter-ping overlap in Figure 12 and summarised in Figure 14a. When the phase centres are either maximally overlapping or misaligned between pings $\{\mu_{\mathrm{w}} \in [4.00, 3.50]\}$, the temporal registration significantly reduces the mean error and has minimal effect on error standard deviation. However, in the case of $\mu_{\mathrm{w}} = 3.75$ phase centres, this is only true when the cubic kernel is used. The reason for this is visible in Figure 10a; in the vicinity of 3.75 overlapping phase centres, the temporal registration reduces the bias for the cubic kernel, but increases it for the Gaussian kernel. Considering the high variability case in Figures 13 and summarised in 14b, a drastic reduction in mean end-of-track error is seen in all cases when the temporal registration is applied. Furthermore, using the Bayesian coherence estimation and cubic interpolation kernel, the standard deviation of the end-of-track error is also significantly reduced.

The percentage improvements in the mean and standard deviation of the end-of-track errors for each of the random walks when comparing the gold standard method with the proposed method are given in Table II, with the comparison made against results of the proposed method derived from both the point-scatterer and van-Cittert Zernike simulations. For the low variability case, we demonstrate reductions in mean end-of-track error of at least 48.5%, with minimal effect on the error standard deviation. In the high variability case, we demonstrate a reduction in end-of-track error of at least 79.8%, while also reducing the error standard deviation by approximately 30%.

VI. Conclusion and Further Work

Three methods for reducing the bias in along-track micronavigation have been developed and evaluated using simulated raw echo data from a point-scatterer simulation and simulated coherence estimates using the pulse-

	Comparison simulation		Reduction in mean end-of-track error (%)		Reduction in end-of-track error standard deviation (%)	
			Point scatterer	van-Cittert Zernike	Point scatterer	van-Cittert Zernike
	μ_w	σ_w				
High variability	4.00	0.04	99.5	87.0	2.7	-14.5
	3.75	0.04	57.9	48.5	-0.5	-12.8
	3.50	0.04	90.8	82.8	10.9	18.6
Low variability	4.00	0.40	97.0	85.9	34.0	30.4
	3.75	0.40	97.2	79.8	31.5	29.2
	3.50	0.40	95.3	81.2	29.4	29.3

TABLE II: A summary of the percentage reduction in the mean and standard deviation of the end-of-track error, comparing the gold standard method to the proposed error reduction methods across all random walks considered and against both point scatterer and van-Cittert Zernike simulation methods.

echo formulation of the van-Cittert Zernike theorem. The bias reduction methods developed comprise a temporal registration of redundant signals prior to coherence estimation, Bayesian coherence estimation, and the use of an improved interpolation kernel. Combined, these methods are shown to reduce along-track micronavigation bias by 48.5 - 99.5%, while reducing the error standard deviation by up to 34%. However, in this study the effect of non-ideal geometries such as inter-ping motion normal to the array axis and relative inclination of the seafloor have been neglected, and only flat seafloors with scattering amplitudes drawn from a negative binomial distribution have been considered. Therefore, further work is required in order to investigate these potential bias sources and fully realise the navigation potential of SAS systems.

Nevertheless, the new bias reduction methods described in this paper are an important development towards enabling SAS systems to be used as effective, high precision and accuracy aiding sensors for navigation of AUVs. This will enable longer underwater transits, improved geolocation accuracy of seafloor imagery, and allow repeated passes to be made with greater accuracy for improved coherent change detection. Furthermore, the temporal registration, Bayesian coherence estimation and improved interpolation kernel described have potential to be adapted to improve the performance of conventional downward-looking CVL systems.

ACKNOWLEDGEMENT

This research made use of the Balena High Performance Computing (HPC) Service at the University of Bath, and was funded by the Office of Naval Research under Grant No. N00014-19-1-2452. Figures use colours provided by [36], [37].

REFERENCES

[1] IXblue. (2020) Phins Subsea. [Online]. Available: https://www.ixblue.com/products/phins-subsea

[2] F. R. Dickey and M. M. Santa, "Final Report on Anti-Clutter Techniques," General Electric Co. Report R65EMH37, Tech. Rep., 1953.

[3] F. R. Dickey, "The correlation aircraft navigator, a vertically beamed Doppler radar," in *Proceedings of the National Conference on Aeronautical Electronics*. Institute of Radio Engineers, 1958, pp. 403–468.

[4] F. R. Dickey and J. A. Edward, "Velocity measurement using correlation sonar," in *IEEE Position Location and Navigation Symposium*, San Diego, USA, 1978, pp. 225–264.

[5] F. R. Dickey. (1981) Velocity measuring correlation sonar. [Online]. Available: https://patents.google.com/patent/US4244026A/en

[6] M. Pinto, "Long Term Accuracy of Synthetic Aperture Sonar Micronavigation using a Displaced Phase Centre Antenna," in *Proceedings of the MTS/IEEE OCEANS Conference*, Charleston, 2018.

[7] P. Gough and M. Miller, "The SAR map-drift algorithm extended for a multi-hydrophone SAS," in *Proceedings of the MTS/IEEE OCEANS Conference*, 2003, pp. 2427–2432.

[8] J. Dillon, "Aided Inertial Navigation in GPS-denied Environments Using Synthetic Aperture Processing," DRDC, Tech. Rep. DRDC-RDDC-2016-C200, 2016.

[9] G. Carter, C. Knapp, and A. Nuttall, "Statistics of the estimate of the magnitute-coherence function," *IEEE Transactions on Audio and Electroacoustics*, vol. 21, no. 4, pp. 388–389, Aug. 1973.

[10] R. Touzi and A. Lopes, "Statistics of the Stokes parameters and of the complex coherence parameters in one-look and multilook speckle fields," *IEEE Transactions on Geoscience and Remote Sensing*, vol. 34, no. 2, pp. 519–531, Mar. 1996.

[11] R. Touzi, A. Lopes, J. Bruniquel, and P. W. Vachon, "Coherence estimation for SAR imagery," *IEEE Transactions on Geoscience and Remote Sensing*, vol. 37, no. 1, pp. 135–149, 1999.

[12] D. C. Brown, "Modeling and Measurement of Spatial Coherence for Normal Incidence Seafloor Scattering," PhD thesis, The Pennsylvania State University, 2017.

[13] A. P. Lyons, J. L. King, and D. C. Brown, "Effects of reverberation and noise on the estimation of synthetic aperture sonar multi-look coherence," *Proceedings of the Institute of Acoustics*, vol. 40, pp. 91–98, 2018.

[14] D. C. Brown, I. D. Gerg, and T. E. Blanford, "Interpolation Kernels for Synthetic Aperture Sonar Along-Track Motion Estimation," *IEEE Journal of Oceanic Engineering (Early Access)*, 2019.

[15] J. Groen, "Adaptive motion compensation in sonar array processing," PhD thesis, Technische Universiteit Delft, 2006.

[16] J. W. Oeschger, "Estimating Along-Track Displacement Using Redundant Phase Centers," *Proceedings of the Institute of Acoustics*, vol. 28, pp. 160–167, 2006.

[17] D. A. Cook, "Synthetic Aperture Sonar Motion Estimation and Compensation," Master's Thesis, Georgia Institute of Technology, 2007.

[18] W. W. J. Bonifant, "Interferometic synthetic aperture sonar processing," Master's thesis, Georgia Institute of Technology, 1999.

[19] D. C. Brown, A. P. Lyons, and D. A. Cook, "Spatial coherence theory and its application to synthetic aperture systems," *Proceedings of the Institute of Acoustics Conference on Synthetic Aperture Sonar and Synsthetic Aperture Radar*, vol. 36, pp. 104–111, 2014.

[20] D. C. Brown and A. P. Lyons, "Velocity estimation using spatial coherence of sea floor reverberation," *Proc. 1st Intl. Conf. and Exhibition on Underwater Acoustics*, pp. 573–581, 2013.

[21] M. Born and E. Wolf, *Principles of Optics: Electromagnetic Theory of Propagation, Interference and Diffraction of Light*. Cambridge University Press, 1997.

[22] G. Carter and A. Nuttall, "Statistics of the estimate of coherence," *Proceedings of the IEEE*, vol. 60, no. 4, pp. 465–466, 1972.

[23] J. Pearson, "Computation of Hypergeometric Functions," Masters, University of Oxford, 2009.

[24] M. Pinto. (2001) Method of resetting sonar images using secondary antenna. [Online]. Available: https://patents.google.com/patent/US6240050B1

[25] B. W. Thomas, A. J. Hunter, and S. Dugelay, "Phase Wrap Error Correction by Random Sample Consensus With Application to Synthetic Aperture Sonar Micronavigation," *IEEE Journal of Oceanic Engineering*, pp. 1–15, 2020.

[26] T. H. Nguyen, M. Chabah, and C. Sintes, "Correlation bias analysis - A novel method of sinus cardinal model for least squares estimation in cross-correlation," *OCEANS 2015 - MTS/IEEE Washington*, 2016.

[27] T. E. Blanford, D. C. Brown, and R. J. Meyer, "Measurements and models of the correlation of redundant spatial coherence measurements for the incoherently scattered field," *The Journal of the Acoustical Society of America*, vol. 146, no. 6, pp. 4224–4236, 2019.

[28] M. R. Foster and N. J. Guinzy, "The coefficient of coherence: Its estimation and use in geophysical data processing," *Geophysics*, vol. 32, no. 4, pp. 602–616, Aug. 1967.

[29] J. O. Berger, *Statistical Decision Theory and Bayesian Analysis*, ser. Springer Series in Statistics. New York, NY: Springer New York, 1985.

[30] A. Bellettini and M. Pinto, "Theoretical accuracy of synthetic aperture sonar micronavigation using a displaced phase-center antenna," *IEEE Journal of Oceanic Engineering*, vol. 27, no. 4, pp. 780–789, Oct. 2002.

[31] WolframAlpha. WolframAlpha. [Online]. Available: www.wolframalpha.com

[32] A. Bellettini and M. A. Pinto, "Design and Experimental Results of a 300-kHz Synthetic Aperture Sonar Optimized for Shallow-Water Operations," *IEEE Journal of Oceanic Engineering*, vol. 34, no. 3, pp. 285–293, 2009.

[33] WolframAlpha. WolframAlpha. [Online]. Available: www.wolframalpha.com

[34] D. C. Brown, S. F. Johnson, and D. R. Olson, "A point-based scattering model for the incoherent component of the scattered field," *The Journal of the Acoustical Society of America*, vol. 141, no. 3, pp. EL210–EL215, 2017.

[35] S. Dugelay and V. Myers, "A correlated K-distributed model for seabed reverberation in synthetic aperture sonar imagery," *Proceedings of the Institute of Acoustics*, vol. 32, no. PART 4, pp. 163–168, 2010.

[36] S. Cobeldick. ColorBrewer: Attractive and Distinctive Colormaps. [Online]. Available: https://github.com/DrosteEffect/BrewerMap

[37] A. Biguri. Perceptually uniform colormaps. [Online]. Available: https://www.mathworks.com/matlabcentral/fileexchange/51986-perceptually-uniform-colormaps